13th International Conference on Greenhouse Gas Control Technologies, GHGT-13, 14-18 November 2016, Lausanne, Switzerland

Using sensitivities and vertical-equilibrium models for parameter estimation of CO_2 injection models with application to Sleipner data

Halvor Møll Nilsen[a,*], Stein Krogstad[a], Odd Andersen[a,b], Rebecca Allen[a], Knut-Andreas Lie[a]

[a]SINTEF ICT, Applied Mathematics, PB 124 Blindern, N-0341 Oslo, Norway
[b]Department of Mathematics, University of Bergen, Bergen, Norway

Abstract

A key part of planning CO_2 storage sites is to devise a monitoring strategy with proper modelling support. Herein, we show how a simulation framework that incorporates adjoint-based sensitivities can be combined with time-lapse seismics to update forecast models of the migrating plume, investigate the measurability of model parameters, and assess the effect of acquiring new measurements (value of information). In particular, we show how the sensitivities in measured quantities with respect to parameters can guide the choice of whether additional data should be obtained or not. To this end, we us singular value decomposition to find determine the model parameters that are best constrained with respect to the measured data, or, viewed alternatively, the parameters that has the largest influence on the mismatch between measured and simulated quantities. Other measurements like uplift data and gravitational data can also be used in our inversion algorithm.

We apply the methodology to the Sleipner benchmark model. A large number of researchers have used plume data to better understand the flow physics and challenge assumptions made previously regarding the model properties. In particular, the parameters for the flow model are uncertain and have been topic of discussion in the literature. Using a vertical-equilibrium simulator, we show that Darcy flow adequately describes the physics of the CO_2 injection and migration. Adjoint-based sensitivities are used to efficiently minimize the mismatch between observations and simulations in an optimization loop giving plausible changes in topography, permeability, CO_2 density, porosity, and injection rates. However, since the minimization of the misfit is not unique, we investigate the Hessian of the misfit function for a reduced set of parameters. By considering the eigenvalue decomposition of this Hessian, we are able to identify its (approximate) null space, i.e., the combinations of parameter perturbations that do not affect plume migration. Similarly, by considering the complementary subspace, we identify the reduced set of parameter combinations that are sufficient to obtain a match. As a result, we obtain a parametrized family of (locally) optimal solutions to the minimization problem, i.e., a family of models that all match the observed data. We also investigate the effect of observation frequency on our model matching methodology, and conclude that for the model considered, frequent seismic measurements are not required to obtain adequate matched models however it give more accurate estimates of the top surface.

---

* Corresponding author. *E-mail address*: HalvorMoll.Nilsen@sintef.no

1. Introduction

The Norwegian Continental Shelf offers enormous volumes of potential storage capacity for CO_2 in saline aquifers [1]. To enable large-scale CO_2 storage, prospective operators need effective monitoring strategies for detecting potential leakages and other undesired effects such as uplift and subsidence. This will require a combination of seismic and non-seismic prospecting technologies, whose raw observation data should be assimilated into forecast models to confirm that the CO_2 plume is behaving as expected and provide support for decision making and remediation planning in the case of unpredicted events. We believe that one can design combined monitoring–forecast strategies that are both robust and efficient by utilizing depth-integrated flow models that rely on an assumption of vertical equilibrium and inversion strategies localized to the storage aquifer. Our main argument for this is that the fluid dynamics of CO_2 storage is conceptually simple in the sense that large density differences between the injected CO_2 and the resident brine will tend to introduce well segregated flow some distance away from the injector, in particular for aquifers with good-quality sand, which are among the most likely candidates for large-scale storage. The evolution of thin CO_2 plumes can be accurately described by depth-integrated models assuming vertical equilibrium. In the resulting models, differences and the topography of the top seal are the main driving forces that determine the evolution of the interface between CO_2 and brine.

This interface will act as a strong reflector for seismic waves and is therefore a quantity that can be measured directly using multiple seismic surveys. Seismic wave propagation through the overburden should remain invariant across repeated surveys and differences in observed travel times and amplitudes can therefore be attributed to movement of fluids. By making model assumptions of how changes in pressure and fluid saturations and compositions affect the seismic responses, one can also invert time-lapse seismics to update petrophysical properties of the geological model [2,3]. Traditionally, seismic inversion is utilized to constrain the aquifer modeling. That is, you acquire time-lapse seismic data, which can be inverted to determine changes in reservoir properties that minimize the misfit between observed and simulated responses. However, it is also possible to use the flow model to constrain the seismic inversion so that the form of the inverted interface can be explained by the pertinent flow physics. Likewise, one can use the flow model to investigate the measurability of model parameters, and assess the effect of acquiring new measurements (value of information).

To start investigating these idea, we will herein consider the Sleipner injection, which is an ongoing CO_2 storage project located in the Norwegian North Sea. Since 1996, approximately 15 Megatonnes (Mt) of CO_2 have been injected [4] for the purpose of long-term storage. A benchmark model, first presented in [5], was established to study CO_2 injection and migration at Sleipner. This benchmark includes a geological model interpreted from seismic maps, rock and fluid properties, and CO_2 entry rates; see Figure 3.

Several attempts have been made to model the CO_2 flow behavior at Sleipner, particularly its accumulation and migration under the caprock of the geological formation's ninth layer [4–12]. A problem commonly encountered is that uncalibrated simulations produce a poor match to the observation data which have been determined by seismic imaging [5,10,12]. In particular, the narrow northward-reaching finger of the 2008 plume is difficult to simulate because CO_2 spills out along the southern portion of the caprock's main structural trap before enough can be contained and channeled northwards (see Figure 6 later in the paper). It has already been suggested by others [10,12] that the nature of the caprock could be cause for a poor match and deserves further study. However to date, we have not seen a detailed assessment of how the caprock topography influences the plume matching efforts.

An important motivation of our work is the observation that the Sleipner grid topography cannot yield the CO_2 plume outlines which are obtained by seismic imaging. We demonstrate this point in Figure 1. To better understand the figure, you can think of water flow downward in a terrain as an inverted analogue of CO_2 migrating upward under a sealing caprock. Then, CO_2 accumulating under the caprock topography will be analogous to the gradual filing of a lake, so that the plume outline superimposed on the surface grid describing the interface between the aquifer and the sealing caprock (henceforth called top-surface grid) should form a planar shoreline.

However, the red line in Figure 1 illustrates that the 2008 plume outline superimposed onto the benchmark's top-surface grid does not form a flat spill-point, and is thus physically unrealistic.

Aspects of the Sleipner benchmark are currently under debate, in particular which modeling method can best capture the flow physics, and variants of the proposed model properties. Two main approaches have emerged to model the flow physics at Sleipner, namely percolation [4,7–9] and Darcy-flow [6,10,12]. Use of the traditional
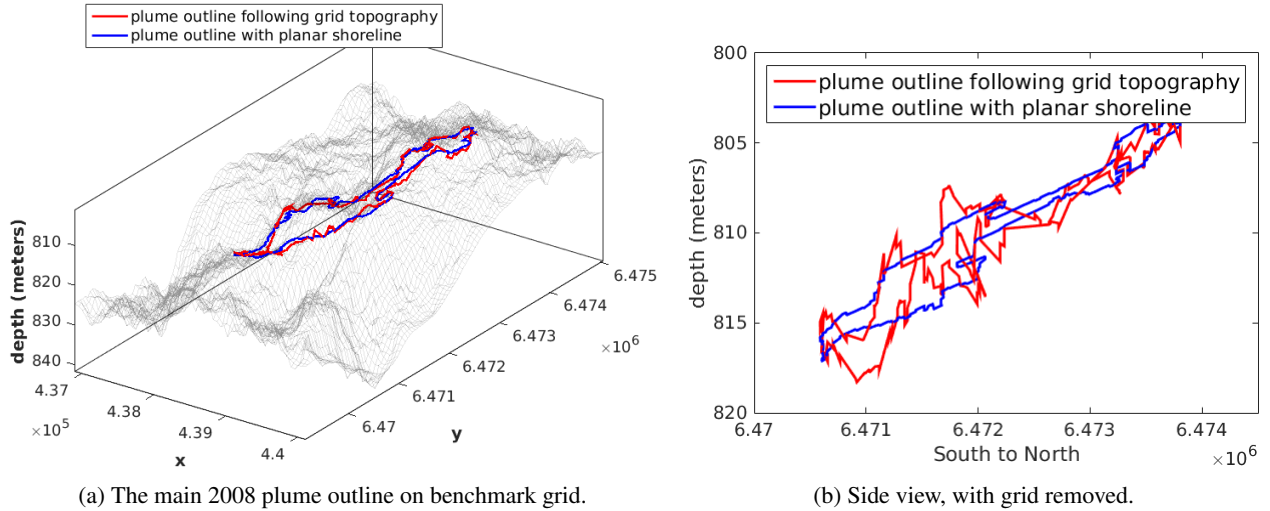
(a) The main 2008 plume outline on benchmark grid.

(b) Side view, with grid removed.

Fig. 1: Mismatch between CO_2 plume data and caprock topography. The 2008 plume outline (red line) is plotted on top of the benchmark grid, as if it sits under the topography of the caprock. For the plume outline to be physically realistic, the elevations of the plume outline should form the shoreline of a planar surface, as shown by the blue line.

Darcy-based approach has been criticized, despite the fact that several works [10,12] have shown that the flow physics can be adequately modeled by Darcy flow in combination with model calibration. Such a calibration is necessary: there is large uncertainty associated with the geological and fluid models, and various authors have used models that deviate quite significantly. For example, [6] uses a grid model that differs from the publicly available grid. Likewise, the first Sleipner benchmark [5] assumes a CO_2 density of 760 kg/m^3, whereas the model presented in [4,8] assumes warmer temperature which leads to a CO_2 density of 355 kg/m^3, almost half of the benchmark's original density.

By incorporating this new understanding of the CO_2 density in a vertical-equilibrium simulator using an open-source software (MRST-co2lab) [13,14], we show that Darcy flow adequately describes the physics of the CO_2 injection and migration. This is demonstrated by using adjoint-based sensitivities to match simulation output to measurements of the time dependent plume. The model modifications consist of plausible changes in topography, permeability, CO_2 density, porosity, and injection rates. All of these parameters for the flow model are uncertain and have been a topic of discussion in the literature.

Furthermore, we show both from the numerical sensitivities and from the model equations that the parameters can be divided into three groups, where caprock governs the shape of the plume outline, CO_2 density and permeability govern the shape of the CO_2–brine contact, and injection rate and porosity affect the volume of the plume. By using the sensitivities obtained from the adjoint simulation, we are able to efficiently minimize the mismatch between observations and simulations in an optimization loop.

Finally, we discuss how the modelling framework can be extended to include uplift data based on the mechanical responses and gravity data based on gravitational changes. Using the sensitivities, we discuss in which situation different measurements can be utilized to give new information about the physical model.

2. Methods

2.1. Governing equations – Darcy-based approach

The basic mechanisms of CO_2 injection and migration can be modeled using two components, water (w) and gas (g), which at aquifer conditions will appear in an aqueous and a supercritical (liquid) phase, respectively. The flow dynamics is described by mass conservation,

$$\frac{\partial(\phi\rho_\alpha s_\alpha)}{\partial t} + \nabla \cdot \rho_\alpha \mathbf{u}_\alpha = \rho_\alpha q_\alpha, \qquad \alpha = w, g, \tag{1}$$

where ϕ is the porosity, s_α is the fluid saturation, ρ_α the fluid density, $\mathbf{u}_\alpha$ the fluid velocity, q_α the volumetric flux caused by any source or sink, and α denotes the fluid phase. The fluid velocity is given by Darcy's equation,

$$\mathbf{u}_\alpha = -k\lambda_\alpha(\nabla p_\alpha - \rho_\alpha \mathbf{g}), \tag{2}$$

where k is the absolute rock permeability; $\lambda_\alpha = k_{r\alpha}/\mu_\alpha$ is the fluid mobility, where $k_{r\alpha} = k_{r\alpha}(s_w)$ and μ_α denote the relative permeability and fluid viscosity, respectively; p_α is the pressure; and $\mathbf{g}$ is gravitational acceleration. The sum of the saturations are equal to unity, and fluid mobilities as well as the capillary pressure (p_c) are expressed as functions of water saturation,

$$s_w + s_g = 1, \tag{3}$$

$$\lambda_\alpha = \lambda_\alpha(s_w), \tag{4}$$

$$p_c = p_n - p_w = P_c(s_w). \tag{5}$$

We notice that the solution in term of s_α and p_α is invariant for the family of parameters

$$\phi = c\bar{\phi}, \quad k = c\bar{k}, \quad q_\alpha = c\bar{q}_\alpha, \tag{6}$$

where c is a positive constant, limited such that $\phi, \bar{\phi} \in [0, 1]$. Furthermore, in the case when all the parameters are independent of pressure, the solution

$$s_\alpha = \bar{s}_\alpha, \quad p_\alpha = c\bar{p}_\alpha \tag{7}$$

is valid for

$$k = \frac{1}{c}\bar{k}, \quad \rho_\alpha = c\bar{\rho}_\alpha, \quad P_c(s_w) = c\bar{P}_c(\bar{s}_w). \tag{8}$$

The capillary condition in (8) is trivially fulfilled when capillary pressure is negligible, but also in the vertically integrated models we will introduce below, in which P_c is proportional to $\Delta\rho$. In either case, this means that there exists a one-parameter family of input variables that give the same pressure and saturation in the general case, and one extra family of solutions that give the same saturation in the limit of incompressible flow. The above discussion did not discuss boundary conditions. The first scaling assumes that all rate conditions at the boundary scale the volume rates and no other modifications are needed since the pressure stays the same. The second scaling is not valid for pressure boundary conditions, but in the case of hydrostatic boundary conditions, an alternative scaling for pressure and density,

$$p_w = c\bar{p}_w + \bar{p}_h, \quad \rho_w = \bar{\rho}_w, \quad \rho_g = c(\bar{\rho}_g - \bar{\rho}_w) + \bar{\rho}_w, \tag{9}$$

gives an invariant solution in which $\bar{p}_h$ fulfills the hydrostatic boundary conditions and $\nabla\bar{p}_h - \bar{\rho}_w \mathbf{g} = 0$. Here, $\bar{p}_w$ is the deviation from hydrostatic pressure for the solution of the system with $c = 1$, which is zero on the boundary.

2.2. Vertically-averaged models

The system (1)–(5) consist of the governing equations in their basic 3D form. Herein, we will rely on an alternative upscaled 2D form obtained by using depth integration (vertical averaging) in combination with an assumption of vertical equilibrium. This has been shown to be a very good physical approximation for CO_2 injection into large homogeneous aquifers with relatively high permeability. In the following calculation we assume a sharp interface to make our discussion clearer, but our simulation code, results, and overall methodology do not depend on this choice. The result of vertical averaging is a set of equations that are similar to (1)–(5), except that each variable and parameter now is replaced with its vertically-averaged counterpart. For brevity, we omit the full formulation of the vertically-averaged equations here, and readers are referred to [6,10,13] for details. Using CO_2 plume thickness (or *height*) h under the caprock as a variable in the incompressible limit, the flow equations can be written in the fractional form as

$$\begin{aligned} \mathbf{u}_t &= -\lambda_t(h)k\Big(\nabla p_i - [\rho_g f_g(h) + \rho_w f_w(H - h)]g\nabla(z_t + h)\Big) \\ &= -\lambda_t(h)k\Big(\nabla p_i - [\rho_w - \Delta\rho f_g(h)]g\nabla(z_t + h)\Big), \end{aligned} \qquad \nabla\mathbf{u}_t = q_t, \tag{10}$$

$$\phi\frac{\partial h}{\partial t} + \nabla f(h)\Big(\mathbf{u}_t - k\Delta\rho\lambda_g(h)\lambda_w(H - h)g\nabla(z_t + h)\Big) = q_g. \tag{11}$$
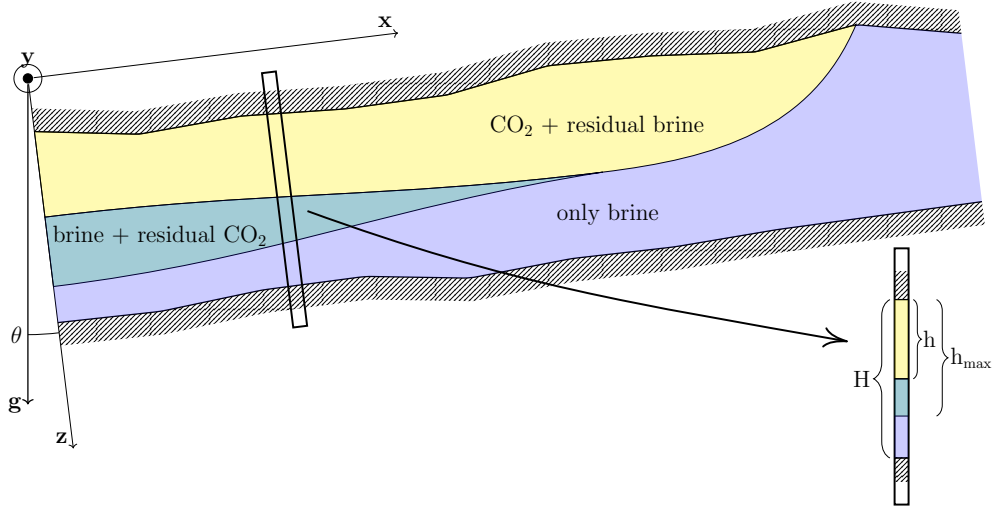
Fig. 2: The layered structure of CO_2 in an aquifer with good injection properties. The basic quantities tracked by a VE solver are shown in the right corner. Here, h is the distance from the caprock to the interface dividing flowing and stationary CO_2, h_{max} is the distance to the maximal depth of capillary trapped CO_2, while H is the height of the aquifer layer.

The first equation is Darcy's law for total volume flux $\mathbf{u}_t$ and the local conservation of volume, where p_i is the pressure at the interface between the fluids, $\Delta\rho = \rho_w - \rho_g$ is the fluid's density difference, H is the total thickness of the aquifer, and z_t is the depth of the top surface. The second equation is the conservation of mass, (i.e., conservation of volume for incompressible flow) of CO_2, where $f_g = \lambda_g/[\lambda_w(H - h) + \lambda_g(h)]$ is the fractional flow function for CO_2 and f_w is the corresponding for water. From this equation we recognize the family of invariant solutions in terms of CO_2 heights. First, any scalar multiplication of porosity, permeability, and volume rates as in (6) is solution invariant. Likewise, we can scale the equations in the limit of no compressibility using (9). With a small modification of (10), we see that in the case of hydrostatic pressure boundary conditions the change in the hydrostatic head of water at the interface, $p_i - g\rho_w(z_t + h)$, is the new scaled pressure instead of the full scaling of all pressures as in equation (7),

$$\Delta\rho = c\Delta\bar{\rho}, \quad p_\alpha = c\bar{p}_\alpha, \quad k = \frac{1}{c}\bar{k}. \tag{12}$$

Two aspects of the Sleipner benchmark model make it preferential to apply vertical-averaging when solving the governing flow equations. Firstly, the flow dynamics in Layer 9 is characterized by gravity-segregation: this segregation occurs because the CO_2 phase is less dense than the surrounding pore water, and thus sits right beneath the caprock due to buoyancy forces; see Figure 2. Strong gravity segregation takes place in this formation, and the migration of CO_2 is strongly influenced by the topology [5]. Another aspect is that the permeability is higher in the horizontal direction than in the vertical, and thus flow in the vertical direction can be considered instantaneous. Indeed, vertical-averaging, or the vertical-equilibrium (VE) method, has been used in several works (i.e., [5,6,10]) to model the Sleipner benchmark. In [6], it was verified that the VE model can capture the flow physics of the Sleipner benchmark by comparing it against the black-oil model in its full 3D form. A few years later, results in [10] again showed that VE models are able to simulate the same migration behavior as captured by full 3D modeling, given a Darcy-based flow model. Using VE is beneficial as it not only reduces the number of grid cells in the model, but also weakens the coupling of pressure and fluid transport, and thus saves a significant amount of computation time.

2.3. Adjoint based gradients

In this section we consider matching uncertain grid and model parameters to observed responses through the use of simulation-based optimization. Let x^n denote the discrete state variables (heights, pressure, and well states) at time t_n, and let F_n denote the corresponding discrete versions of equations (1)–(2) such that

$$F_n(x^{n-1}, x^n) = 0, \ n = 1, 2, \ldots, N, \tag{13}$$

constitute a full simulation given initial conditions x^0. To match simulation output to a set of observed quantities, we augment (13) with a set of model parameters θ^n such that,

$$F_n(x^{n-1}, x^n, \theta^n) = 0, \ n = 1, 2, \ldots, N. \tag{14}$$

The matching procedure consists of obtaining a set of model parameters θ that optimize the fit to observed data, i.e., minimizing a misfit function of the form

$$J = \sum_{n=1}^{N} J_n(x^n, \theta^n). \tag{15}$$

For obtaining gradients of J, we solve the adjoint equations for (14), see [15]. The adjoint equations are given by

$$\left(\frac{\partial F_N}{\partial x^N}\right)^T \lambda^N = -\frac{\partial J_N}{\partial x^N} \tag{16}$$

for the last time-step N, and for $n = N - 1, \ldots, 1$,

$$\left(\frac{\partial F_n}{\partial x^n}\right)^T \lambda_n = -\frac{\partial J_n}{\partial x^n} - \left(\frac{\partial F_{n+1}}{\partial x^n}\right)^T \lambda^{n+1}. \tag{17}$$

Once the adjoint equations are solved for the Lagrange multipliers λ^n, the gradient with respect to θ^n is given,

$$\nabla_{\theta^n} J^n = \frac{\partial J^n}{\partial \theta^n} + \left(\frac{\partial F^n}{\partial \theta^n}\right)^T \lambda^n. \tag{18}$$

In this work, we consider a set of parameters θ constant over time, i.e., $\theta^n = \theta, \ n = 1, \ldots, N$, such that

$$\theta = \{dz, m_q, m_\rho, m_k, m_\phi\}. \tag{19}$$

In the above, m_q, m_ρ, m_k, m_ϕ are scalar multipliers for rate, CO_2 density, and homogeneous permeability and porosity, respectively, while dz is the absolute adjustment in top-surface depth of dimension equal to the number of grid cells.

From the discussion in Section 2.2, an exact solution invariant parameter family (6) is generated by the *basis*

$$\hat{\theta}_1 = \{\mathbf{0}, 1, 0, 1, 1\}. \tag{20}$$

The scaling that gives an invariant saturation in the incompressible limit, follows from

$$k(\rho_w - \rho_g) = C \quad \rightarrow \quad \mathrm{d}m_k\left(\rho_w - \rho_g\right) - \mathrm{d}m_\rho\,\rho_g = 0. \tag{21}$$

This gives the basis vector

$$\hat{\theta}_2 = \{\mathbf{0}, 0, 1, \left(\frac{\rho_w}{\rho_g} - 1\right), 0\}. \tag{22}$$

The two vectors $\hat{\theta}_1$ and $\hat{\theta}_2$ are not orthogonal, but this can be obtained by a redefinition of the parameters. In the case in which the objective function J only depends on saturation (i.e., we only match plume thickness h), these vectors span parameter choices that give indistinguishable objective function values. When the multipliers are evaluated relative to a minimum in J, the vectors $\hat{\theta}_1$ and $\hat{\theta}_2$ are eigenvectors of the Hessian of J with zero eigenvalues.

2.4. Parameter estimation

Given a nonlinear model $y = F(\theta)$, where θ are the model parameters, the calibrated model against measurements $\hat{y}$ is given by the minimum of the objective function

$$J = \left(\hat{y} - F(\theta)\right)^T \left(\hat{y} - F(\theta)\right), \tag{23}$$

if the measurements are assumed to be uncorrelated. For a linear model $F = A\theta$, the above is the traditional least-square estimate, and can be calculated explicitly

$$\tilde{\theta} = (A^T A)^{-1} A^T \hat{y}. \tag{24}$$

In this case, it is the best linear unbiased estimator (BLUE). This is a special case of general least-square estimate, where the assumption is that the model and the measurement process can be modeled by

$$y = A\theta + \epsilon \quad E[\epsilon|A] = 0 \quad Var[\epsilon|A] = \Omega. \tag{25}$$

Here, ϵ is a stochastic variable, $E[\epsilon|A]$ is the conditional mean of ϵ given A, and $Var[\epsilon|A]$ is the conditional variance. The general least-square estimator is then given by the minimization of the objective function

$$J = \left(\hat{y} - F(\theta)\right)^T \Omega^{-1} \left(\hat{y} - F(\theta)\right). \tag{26}$$

This estimator is unbiased, consistent and efficient. Furthermore, it is asymptotically normal with standard deviation approaching

$$nVar(\tilde{\theta} - \theta) \rightarrow (A^T \Omega^{-1} A)^{-1} \tag{27}$$

as the number n of measurements grows. Assuming the stochastic variables are Gaussian, the above estimate can be seen as the value of θ that makes the measured results most probable. This interpretation also suggests a natural regularization in which quadratic changes of the parameters are added as penalties. As such, they can naturally be seen as a result of a trivial predictor and measurement process in the same way with A the identity.

The generalized least-squares estimator only works well when the matrix has full rank and is well conditioned. In the two previous sections, we showed how certain parameter combinations were solution invariant, which in turn correspond to the same values of the plume thickness h. The existence of such non-trivial solution invariant parameter spaces will lead to rank deficiency in A. This can be investigated from the full linear model by singular value decomposition (SVD) of A

$$A = USV', \tag{28}$$

where U and V are unitary matrices and S is a diagonal matrix with non-negative real numbers σ_i on the diagonal, which are referred to as the singular values of A. We will refer to the columns of V as the parameter singular vectors and the column of U as the response singular vectors, when we consider SVD of a sensitivity matrix, since they for a given singular value govern the changes in the parameters which correspond to a given response. From the standard deviation of the estimate, we see that high singular values give low standard deviation for the input variables corresponding to this singular value. Parameter singular vectors corresponding to small singular values indicate combination of parameters that can not be estimated accurately. Seen from the objective function, this corresponds to small eigenvalues of the Hessian at the estimate. Given a linear model with the above singular value decomposition, the objective function can be reformulated in terms of matched parameters and updates by

$$J = (\hat{y} - A\tilde{\theta})^T (\hat{y} - A\tilde{\theta}) + d\theta^T V' S^2 V d\theta \tag{29}$$

where $\theta = \tilde{\theta} + d\theta$, and Hessian $U'S^2U$.

One should note that the SVD decomposition is sensitive to the definition and scaling of the parameters so care has to be taken when variables of different types are considered. On the other hand, the standard deviation of the estimate does not depend on scaling, which shows that the natural scaling in this given setting is the inverse of the covariance of the measurements. That is, for uncorrelated measurements, the right scaling is the standard deviation.

2.5. Our objective function

The previous section introduced a general form of the objective function (23). More specifically, we seek to minimize $J = \sum J_m$ with

$$J_m(h_m) = \sum_{\text{cells}} V(h^m - h^m_{\text{obs}})^2 + \sum_{\text{cells}} \alpha dz^2 V. \tag{30}$$

Here, $m = 1, \ldots, M$ denote the time-instances of the set of *observed* heights h_{obs} (e.g., CO_2 plume thickness data taken from literature, etc.), h are the simulated heights for the given set of parameters θ (19), and V is the volume of the aquifer found below each cell in the 2D top surface grid. Since the top-surface elevation is more uncertain that the plume thickness h, we give dz less weight in calculation of the misfit by setting $\alpha = 1/9$.

Later, we will evaluate the algorithm by matching the model to perturbed simulation output, and assess the sensitivity of the match to the number of time-instances of the data h_{obs}.

2.6. Building a linear model

Traditionally, computing the full linear response model is very expensive, in particular when using full 3D simulation of the plume migration need both a high vertical resolution to resolve the thin plume and high lateral resolution to capture caprock topography. Herein, we will use VE type simulations with adjoint capabilities to make the forward simulation more computationally tractable for models with reasonable lateral resolution. To investigate a complete linear model between the parameters and the plume height, we can use the adjoint method with one objective function for the position of interest defined as $J_i^n = h_i^n$, where h is the plume height and n and i indicate the position in space and time, respectively. Then, the adjoint method can get all derivatives with respect to θ by one backward simulation. Also, the backward simulations for the different space and time points can be performed in parallel and can also reuse the preconditioner or the LU-decomposition of the system matrix since the only differences between the calculations are in the right hand sides. Additionally, information about the response induced by changes in the parameters at different times can be stored. The result is a series of linear relationships,

$$\mathrm{d}h^n = A^n \mathrm{d}\theta. \tag{31}$$

We point out that the backward simulation is linear, which makes this simulation much faster than the forward simulations. In addition, the computation time is less dependent on the particular objective function, which makes load balancing in a parallel framework ideal.

3. The Sleipner Layer 9 (L9) benchmark model

We start by summarizing the details of the benchmark:

- *Fluid and rock properties* We fix the water density to be the same as that given in the benchmark ($\rho_w = 1020$ kg/m³), and use the benchmark's CO_2 density ($\rho_g = 760$ kg/m³) only as a *reference* density since our goal is to calibrate the CO_2 density. We set the fluid viscosities to $\mu_w = 0.0008$ Pa·s and $\mu_g = 0.00006$ Pa·s. Residual saturations of $S_{r,w} = 0.11$ and $S_{r,g} = 0.21$ were included in the benchmark, and while our vertical-equilibrium simulator is able to handle residuals, we neglect them for the purposes of our study since our work is to calibrate the model parameters, i.e., we want to keep things less complicated given the uncertainty associated with the parameters. Other properties we have specified for our compressible-flow model are water compressibility (4.37×10^{-10} Pa) and CO_2 compressibility of 10 times that of water. We note that compressibility will have a minimal impact here. In addition, a pore volume multiplier of 1×10^{-5} bars^{-1} was used, which accounts for the increase in pore volume due to pressure increases. We do not model CO_2 dissolution into water as it is negligible for the time scale of this injection scenario.
- *Injection point and rate* We use the same CO_2 point of entry, coordinates $(0.438516, 6.47121) \times 10^6$, and rates (see Figure 3) as [5]. Initial conditions are set such that there is initially no CO_2 so that the formation is fully saturated with water, which is in hydrostatic balance.
- *Geological grid* The geological model consists of a caprock layer, a shale layer, and a homogeneous sand layer sandwiched in between. These layers make up what is referred to as the *Sand wedge Unit Layer 9* (SUL9), or simply *Layer 9*; see Figure 3. The permeability of the caprock and bottom shale layers are low enough to treat them as impermeable to fluid flow. The sand layer is characterized by an average porosity of 0.3571 and isotropic horizontal permeability (k_x, k_y) of 1.825×10^{-12} m² (1850 mD) [5].
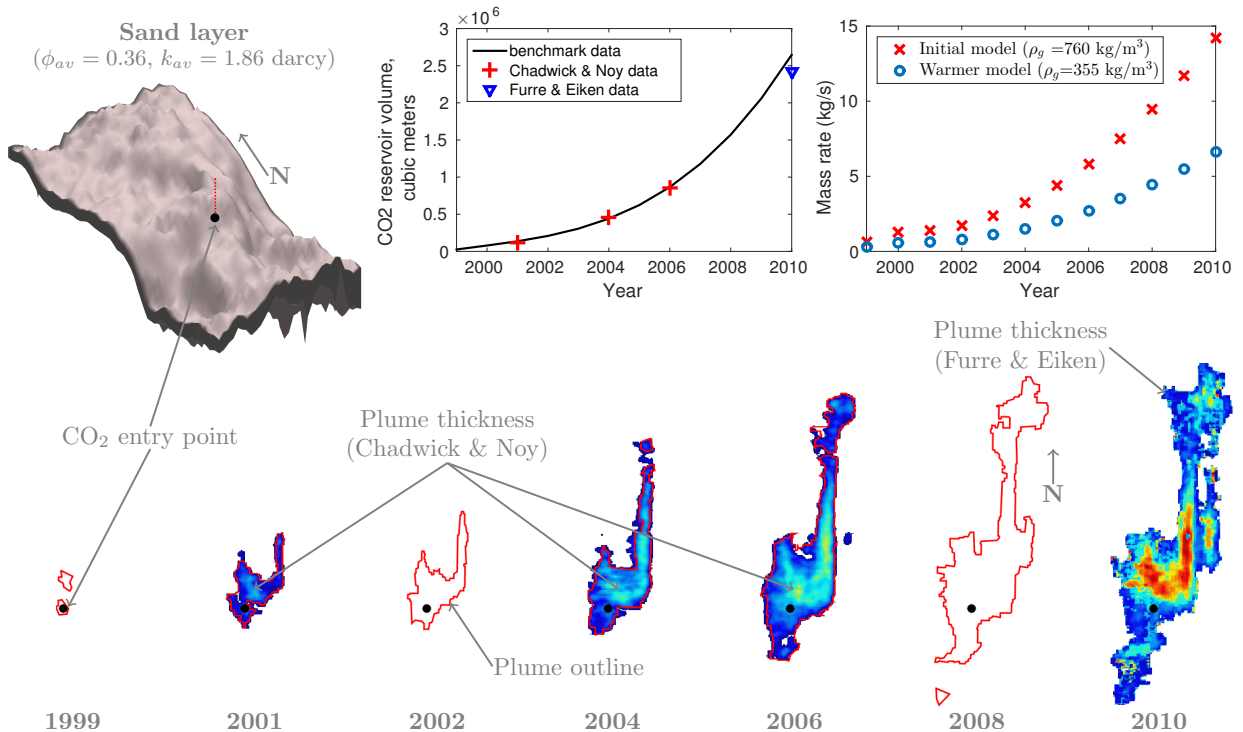
Fig. 3: The Sleipner benchmark (sand layer, entry rates, fluid and rock properties) from [5], and CO_2 plume data taken from Chadwick & Noy [16] and Furre & Eiken [17]. While seismic imaging can estimate the amount of CO_2 volume in Layer 9, the CO_2 mass entry rates depends on the inferred reservoir density; mass rates shown here are with respect to densities of 760 and 355 kg/m^3.

Variants of model parameters. While [5] tabulated what they considered to be the best estimates for the model, variants of the benchmark do indeed exist. The injection rates used in the benchmark represent the amount of CO_2 which is *entering* Layer 9. Sleipner's injection well is located at $(x, y) = (0.438516, 6.47121) \times 10^6$, at a depth of 1010.5 meters below sea level [5]. At this depth, CO_2 enters Layer 1 and is assumed to migrate laterally underneath the caprock of this first layer and then rise upward into each overlying layer until it enters Layer 9. Thus the entry point of CO_2 into Layer 9 is taken as the same coordinate location of the injection well, albeit at a shallower depth. We note that [12] has simulated other possible entry points into Layer 9, and that the *new* Sleipner benchmark [8,9] includes Layer 8 in the geological model, which provides opportunity for simulating CO_2 entry into Layer 9. However, this new benchmark was not released at the time of this work, thus we stick with the entry point given in the earlier benchmark.

The benchmark model provides yearly volumetric CO_2 entry rates into Layer 9 from 1999 and 2009, illustrated in Figure 3. Seismic imaging provides estimates regarding the amount of CO_2 volume accumulating in Layer 9, and the volumetric rate is depicted in Figure 3. The corresponding mass rate of CO_2 entering the layer depends on the inferred reservoir density. If the reservoir density is lower than the 760 kg/m^3 assumed in the original model – such as 355 kg/m^3 as presented in [8,9] assuming a warmer model – the corresponding mass rate of CO_2 entering Layer 9 is also lower, as shown the upper-right plot.

We note that the 1999 plume outline (shown in Figure 3) reveals two areas where CO_2 is entering into Layer 9; the southern most areas is located by roughly the same latitude and longitudinal coordinates as the point of injection in Layer 1. As such, the placement of the CO_2 entry point in Layer 9 could be a valid assumption. However, it is possible that CO_2 begins to enter into Layer 9 at other locations in later years. The start of such an additional entry point, the location, and the rate of entry could have been included as additional parameters in our calibration procedure, but this is left for future work.

Table 1: Impact of time-resolution on simulated match.

	exact	$m = 10$	$m = 2$	$m = 1$
m_k	1.20	1.20	1.14	1.14
m_ϕ	0.75	0.75	0.75	0.75
m_ρ	0.80	0.80	0.79	0.79
e_{dz}		see Figure 4		
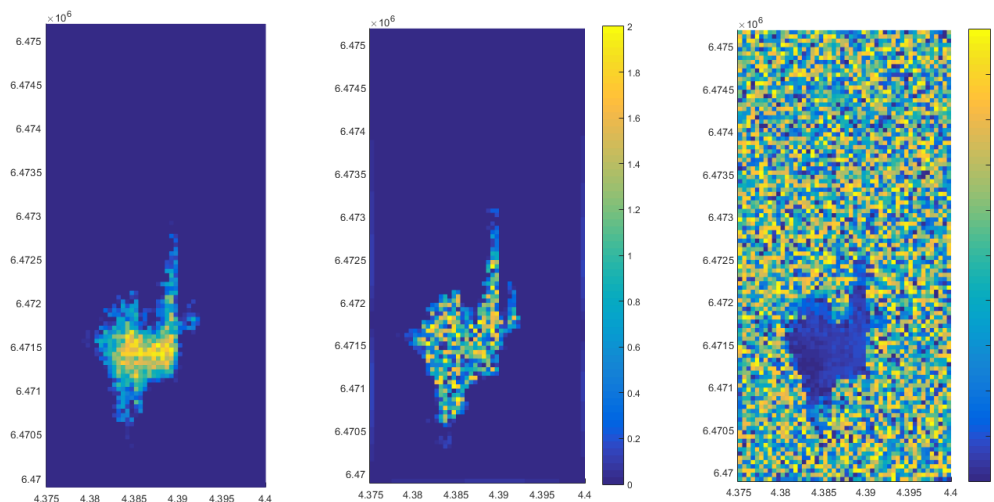
Fig. 4: Plume thickness at end time (left), absolute value of dz-parameters obtained from optimization (middle), and difference in optimized and true dz (right). Units of colorbar is in meters.

Assumed measurements. Four sets of observed plume heights h_{obs} were taken from results published in Chadwick & Noy [16] and Furre & Eiken [17]. From these heights, we determined the corresponding plume volumes at the four observation years. Chadwick & Noy's 2001, 2004, and 2006 volumes match quite closely to the Sleipner benchmark, but there is a slight discrepancy between the benchmark and Furre & Eiken's 2010 volume; see plot of CO_2 reservoir volume in Figure 3. This discrepancy is not surprising given the fact that these studies used different methods to interpret CO_2 plume heights from seismic data.

4. Examples: seismic inversion

4.1. Matching model to perturbed simulation output

To evaluate the algorithm, we attempt to match the *a prior* model to output (*observations*) from a simulation obtained from a set of known model perturbations. In the process of minimizing (30), it is advantageous to determine dependencies between the chosen parameters. This can be done, either through a careful analysis of the governing equations, or through numerically computing the null-space of the Hessian $H(\theta) = d^2 J / d\theta^2$. In particular, we found that for the scalar parameters

$$\text{null}(H(m_q, m_\rho, m_k, m_\phi)) \approx \text{span}\left([1, 0, 1, 1]^T\right). \tag{32}$$

as expected from the discussion in Section 2.1. Hence, any parameter update in this direction has no effect on the misfit objective (30). For the numerical validations, we therefore fix the rate-multiplier to eliminate this null space. For the dz-parameters, it is obvious that those corresponding to cells lying outside the end-time plume will have no effect on the objective. Hence, in evaluating the fit, we limit the match to the reference *plume*-cells.

For this matching example, we use a ten year simulation horizon (1999-2008), and an in-house (preliminary) benchmark grid that was used in [6]. In assessing the sensitivity to the time-resolution of the objective (30), we
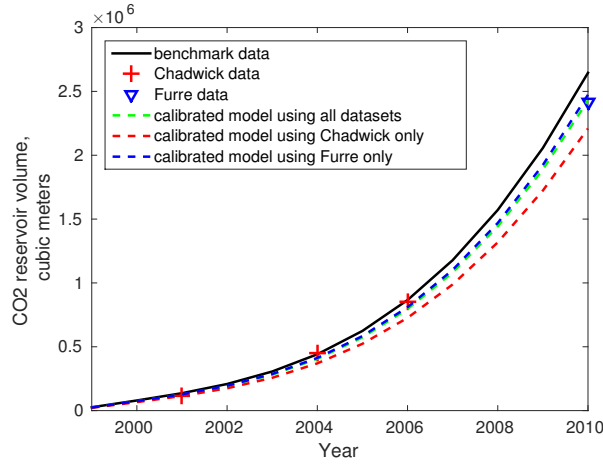
Fig. 5: Comparison of calibrated (cumulative) plume volumes obtained by matching to three different combinations of data.

consider three matching scenarios; once a year (ten instances), every five years (two instances) and a single instance at end of simulation; see Table 1. Results for the matching scenario with ten instances is illustrated in Figure 4, which confirms that our algorithm is able to match *a prior* model output given the fact that the difference between optimized and true *dz* (at *plume*-cells) is essentially zero. We also notice that including more time information helps the algorithm.

However, we also notice that the time information used to calibrate the model may not be consistent with each other. In Figure 5, we see that Chadwick's data fits closer to the benchmark volumes than Furre's data. Calibrating the model using three different sets of data (i.e, only Chadwick & Noy's 2001, 2002, and 2004 data; only Furre & Eiken's 2010 data; all four years worth of data) yields different results. Since our model calibration includes a (scalar) rate multiplier, we do not expect to obtain calibrated injection rates that produce volumes that fit precisely to all four observation years.

## 4.2. Matching plume on Sleipner

We now proceed to match our model to the data described in Section 3 using the objective function describing the misfit between the measurements and the simulated values (30). We minimize this function using the same methods as in [18] given a set of parameters θ in the same way as with the linear least-square theory (24). We use the misfit objective (30) with observed plume heights h_{obs} for the years 2001, 2004, 2006, and 2010 (the first three years of data are taken from [16], and the last year is from [17]). Given a match that minimizes the misfit, see Figure 6, we study the Hessian $H = \frac{d^2 J(\theta)}{d\theta^2}$ excluding dz, and its eigenvalues, which are given

$$H = \begin{bmatrix} -2.1625 & 0.0351 & -0.0446 & 2.2026 \\ 0.0353 & -0.3284 & 0.3707 & -0.4030 \\ -0.0448 & 0.3707 & -0.4264 & 0.4643 \\ 2.2028 & -0.4029 & 0.4642 & -2.6555 \end{bmatrix}, \quad v = \begin{bmatrix} -4.6884 & 0 & 0 & 0 \\ 0 & -0.8816 & 0 & 0 \\ 0 & 0 & 0.0006 & 0 \\ 0 & 0 & 0 & -0.0035 \end{bmatrix}. \quad (33)$$

Here, the Hessian is calculated numerically using adjoint derivatives. We recognize two small eigenvalues as we expect from the discussion in Section 2.1. However, we cannot identify the invariant vectors immediately. In the case of equal eigenvalues, the eigenvectors are not unique. Up to numerical accuracy we consider the eigenvectors corresponding to the two smallest smallest eigenvalues

$$q_3 = [-0.6257, 0.3057, -0.3501, -0.6265]^T, \quad q_4 = [0.0014, -0.7520, -0.6592, 0.0001]^T. \quad (34)$$
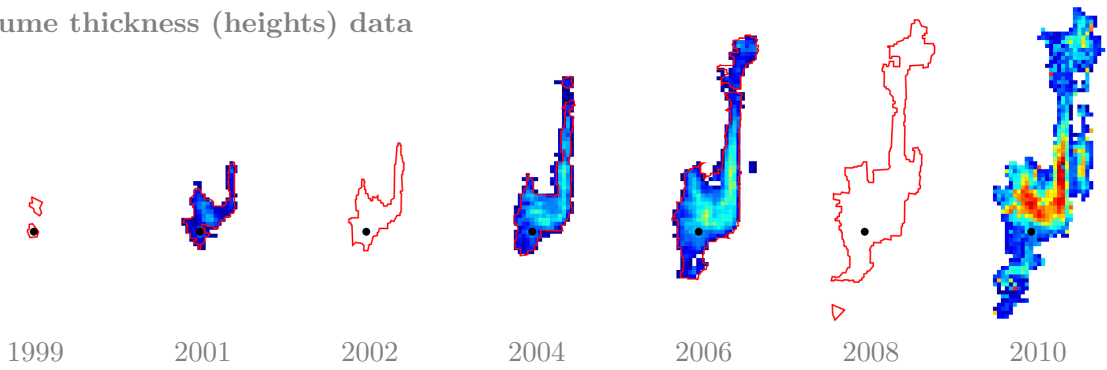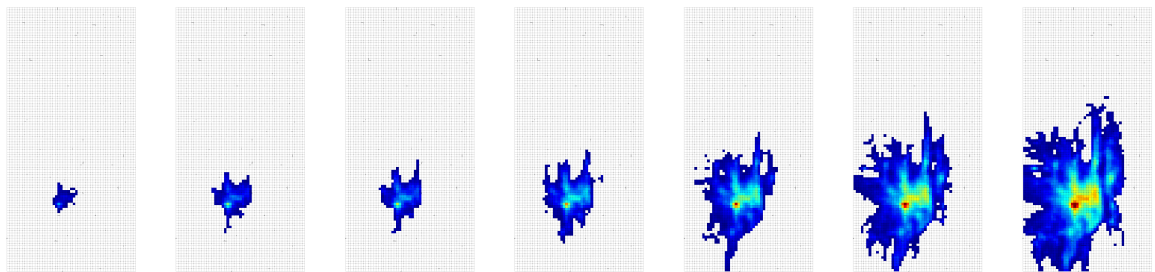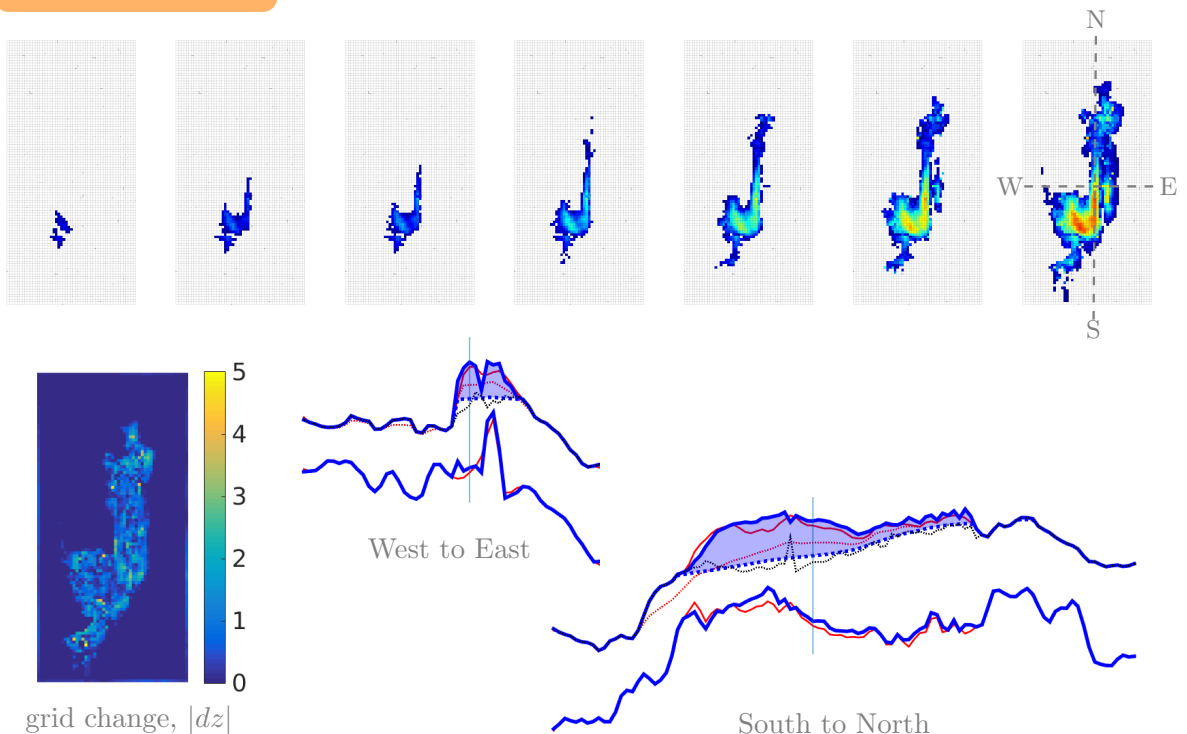
Fig. 6: Evolution of CO_2 plume thickness simulated using the initial benchmark model and a calibrated ($s = 0$) model. Calibration performed using CO_2 height data of years 2001, 2004, and 2006 taken from [16] and CO_2 height data for year 2010 taken from [17]. Color range of plume heights: dark blue to dark red corresponds to 0.1 to 9.77 meters. Grid change is in meters. Side-profiles: red and blue indicate initial and calibrated grid, respectively. Red and blue dashed lines are simulated CO_2-water contact lines, and black dashed line is plume thickness data under calibrated top-surface.

Table 2: A family of calibrated models. Rate multiplier is applied to the benchmark's volumetric rates. Average permeability and porosity are reported here. Thermal gradient is computed from the calibrated densities. These results obtained using q_3, d_3, and d_4.

	q_3			d_3		d_4	
s	-0.5	0	0.5	-0.5	0.5	-0.5	0.5
rate multiplier, m_p	0.59	0.92	1.25	0.92	0.92	1.19	0.65
density (kg/m^3)	565	478	391	657	298	478	478
permeability (darcy)	10.2	12.7	15.1	16.8	8.5	16.3	9.0
porosity	0.24	0.37	0.51	0.37	0.37	0.48	0.27
dz		see Fig 6					
thermal gradient ($°C/km$)	34.9	35.4	35.8	32.8	38.5	35.4	35.4
$k\Delta\rho$ (kg/m)	4.58×10^{-9}	6.79×10^{-9}	9.37×10^{-9}	6.02×10^{-9}	6.04×10^{-9}	8.71×10^{-9}	4.83×10^{-9}

as belonging to the same eigenvalue. We reformulate these eigenvectors to get a new basis for the nullspace of the Hessian

$$d_3 = \frac{\tilde{q}_3}{\|\tilde{q}_3\|}, \quad \text{where} \quad \tilde{q}_3 = q_4 - \frac{q_{4,i}}{q_{3,i}} q_3 = [0, -0.7513, -0.6600, -0.0014]^T, \tag{35}$$

$$d_4 = \frac{\tilde{q}_4}{\|\tilde{q}_4\|}, \quad \text{where} \quad \tilde{q}_4 = q_4 - \frac{q_{4,j}}{q_{3,j}} q_3 = [-1.5380, 0, -1.5206, -1.5413]^T. \tag{36}$$

Here, we can set $i = 1$ or 4 to eliminate the changes in rate and/or porosity and likewise set $j = 2$ to eliminate changes in density. Note the following:

$$\frac{\tilde{q}_{3,2}}{\tilde{q}_{3,3}} = \frac{0.7513}{0.6600} \approx \left(\frac{\rho_w}{\rho_g} - 1\right), \quad \tilde{q}_4 = [-1.5380, 0, -1.5206, -1.5413]^T \propto [1, 0, 1, 1]^T. \tag{37}$$

We recognize d_3, (22), as a basis for the approximate invariant of the system and d_4 as the exact invariance, (20).

By multiplying either of these vectors by some scalar quantity c, we find a family of calibrated models that are capable of producing the same misfit, e.g.,

$$J = J(\theta + s\,d_3), \tag{38}$$

This family is presented in Table 2, and results corresponding to $s = 0$ are illustrated in Figure 6. As indicated by these results, the family of calibrated models includes a higher permeability, lower density, and caprock depth changes (dz) between zero and several meters compared with the initial benchmark model. It is reasonable to adjust caprock depths because plume migration is strongly impacted by the caprock topography, not to mention the fact that the uncertainty associated with these depths is reportedly 5 to 10 meters [5]. Given the matched density, we calculate the corresponding thermal gradient. First we determined the temperature of Layer 9 that corresponds to the calibrated density (assuming hydrostatic pressure conditions) using the open-source *coolprop* package [19], which uses the Span & Wagner equation-of-state [20]. Then, the thermal gradient was found using the benchmark parameters for seafloor temperature (7°C), average depth of Layer 9's top-surface, and an assumed sea depth of 100 meters. We notice that the thermal gradient is very near the benchmark's proposed value of 35.6 °C/km. If we consider the matched result, the most unrealistic change from a physical perspective is the permeability. In our opinion, one of the main uncertainties in the model is the assumed injection point and, in particular, the assumption of a single point. This will not only make a match around the injection point difficult, but also require higher permeability to push the plume in the observed direction than what one would obtain with a more spread-out source. Also as discussed before, using only plume thickness gives a match that is sensitive to parameter changes. Moreover, the data we used were obtained from processed data, which may contain significant noise. Finally, the match was obtained without weighting the mismatch function, which corresponds to assuming equal accuracy of the proposed measurements independent of plume height, see Section 2.4.

4.3. Linear sensitivities to geometry changes

Starting from a matched model on Sleipner described in the previous example, we build the linear sensitivity for the mapping between the input variables θ and the assumed measurements found from the estimations of the plume
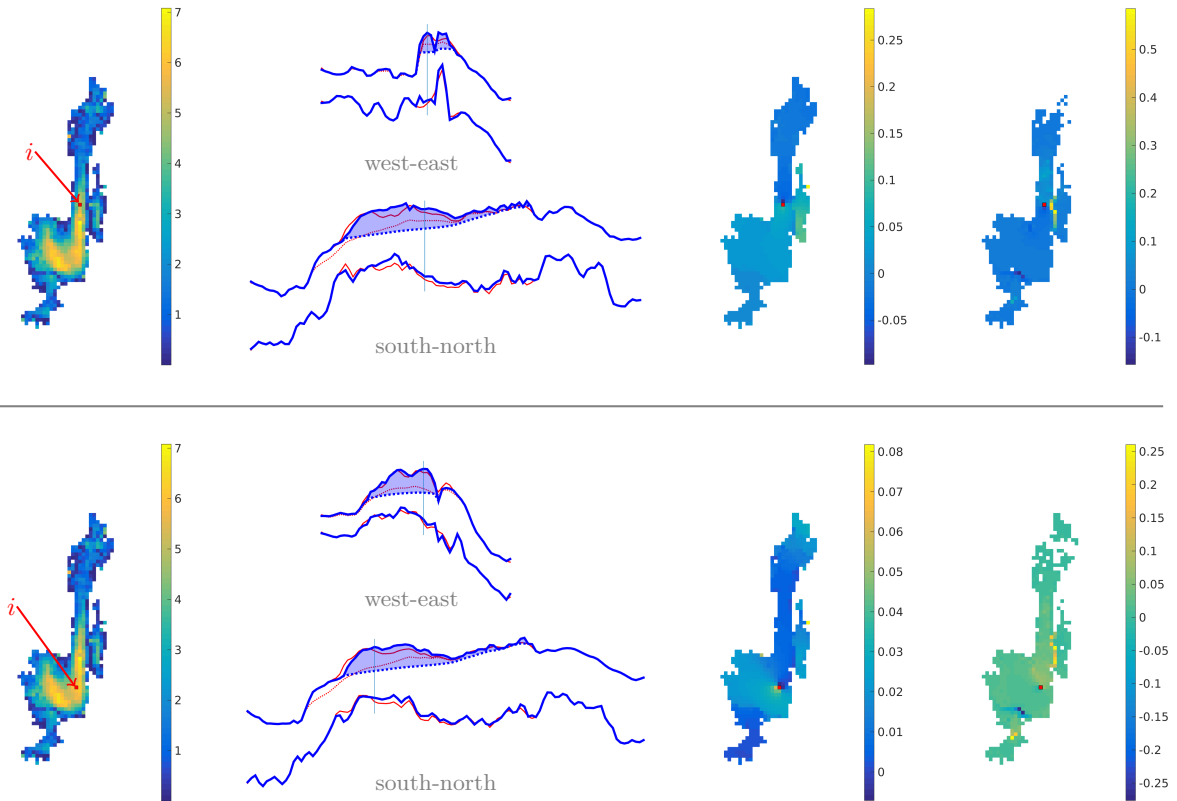
Fig. 7: *Top row, left to right*: CO_2 plume shape and thickness for year 10 (i.e., 2008) with point i located; slices through point i; dh_i/dz_n, where z_n indicates elevation change in the line-crossing and h_i is the CO_2 height for each cell; and dh_n/dz_i, where h_n is the CO_2 height at the line-crossing and z_i the elevation change in the cells. *Bottom row*: same as top row but for a point i that is nearer to the larger part of the CO_2 plume.

heights h_t at a given time. This can be described by the relation

$$dh_t = A_t d\theta, \tag{39}$$

where dh_t is the change in CO_2 thickness from the matched model corresponding to a change $d\theta$ of the parameter from the estimated value. Furthermore, we will describe the sensitivities to top-surface changes by $A_{s,t}$, which gives a relation between the changes in the top surface and the CO_2 thickness, $dh_t = A_{s,t}dz$. Figure 7 shows the change in CO_2 thickness with respect to the change in top-surface elevation for a specific point, and the change of CO_2 thickness at a specific point with respect to different changes in topography. In the top row of Figure 7, the specific point is located in the middle of the northward CO_2 *finger*, or *sand bar*, and towards the start of this sand bar. We see that a change in the top surface downwards (i.e., deeper) will increase the CO_2 thickness before the point and decrease it after, second-right figure. We also clearly identify the regions that will change the CO_2 plume at the point; see right column. Here, the regions related to the spill point in the sand bar can be identified. In the case of the more southern point shown in Figure 7, bottom row, which we notice is less sensitive to changes, the earlier part of the bar is more significant. This is since, in this case, a change in this region will prevent even more CO_2 from entering the bar. Thus the sensitivities identify important features of the model which influence different points, i.e., measurements. A well established technique to identify the most important aspects of an linear model is SVD; see Section 2.4. Figure 8 shows aspects of the SVD decomposition of the spatial related sensitivities. The red line in the top middle panel shows the singular values of this matrix, in which we see a clear plateau. However, if we plot the diagonal part of the sensitivity in space, i.e., how much does a change in elevation influence the CO_2 plume thickness at a given point, we see that for large parts of the plume this is near -1. From a physical point of view, this indicates that $h + z$ is near constant, which one should expect for situation near local equilibrium. Using this information, which indicates
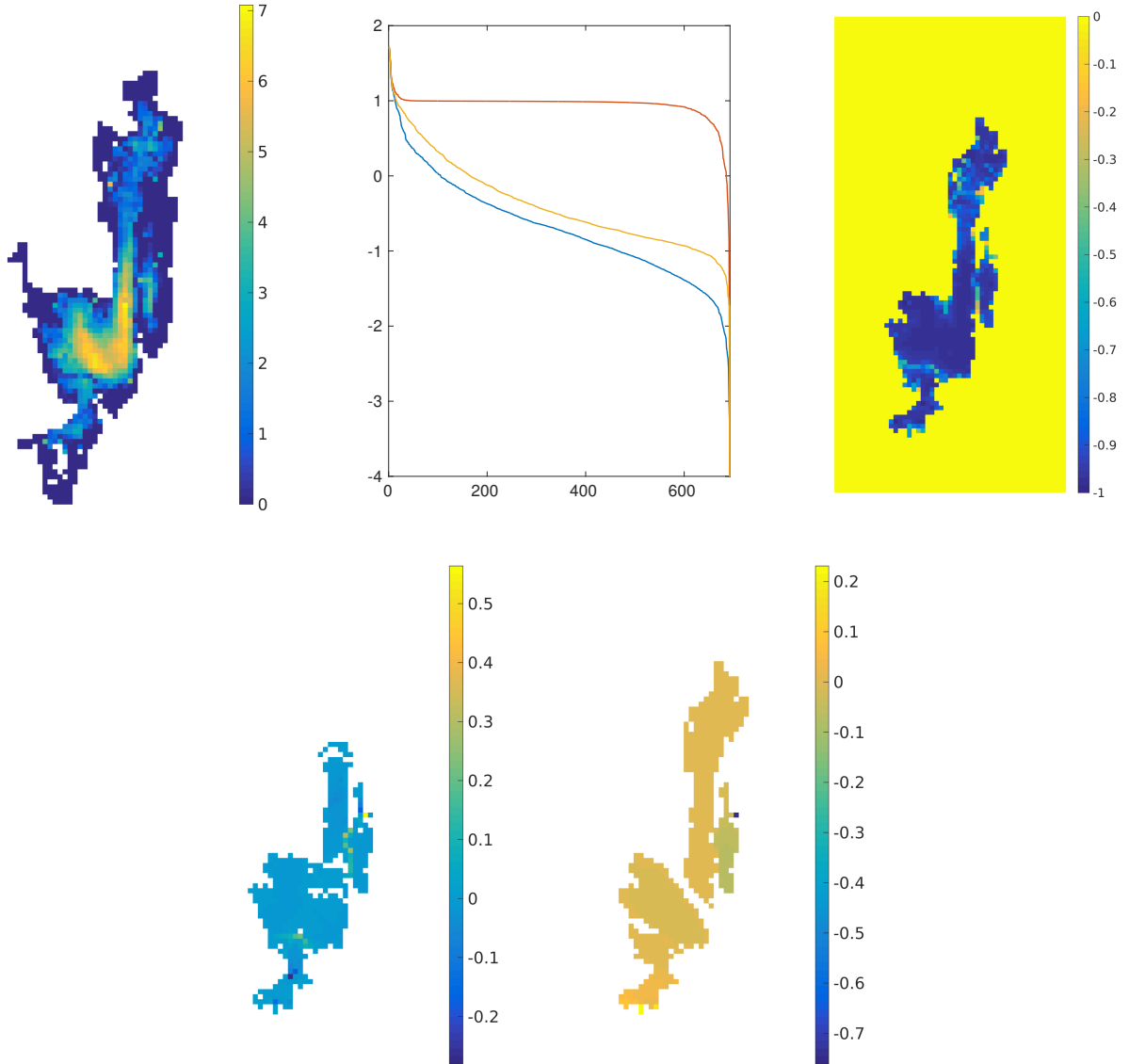
Fig. 8: Different aspects of the sensitivity matrix for year 10 (i.e., 2008). *Top left*: CO_2 plume thickness and shape (colorbar in meters). *Top middle*: singular values of the sensitivity matrix related to elevation change of the top surface. Red line is for the original sensitivity matrix, while blue is for the sensitivity matrix where the diagonal part is neglected. *Top right*: diagonal part of the sensitivity matrix related to elevation change, plotted in space. *Bottom row*: left and right eigenvalue of the modified sensitivity matrix related to the highest singular value.

that the sensitivity is dominated by local contributions, we define two modified matrices corresponding to mappings between parameters and linear combination changes in CO_2 thickness and top surface

$$dh + dz = A_{s,t}^w dz \quad A_{s,t}^w = A_{s,t} - I$$
$$dh + \text{diag}(A_{st})dz = A_{s,t}^w dz \quad A_{s,t}^d = A_{s,t} - \text{diag}(A_{st}). \tag{40}$$

The first mapping, A_{st}^w, can be seen as calculating for the water-CO_2 interface instead of the CO_2 height, while $A_{s,t}^d$ is a mapping that helps separate the local and the global contributions to changes. If we now look at the singular values for A_{st}^w and A_{st}^d, we notice that the decay is much faster. This means that there are a few changes in the top surface that dominate the global changes. This indicates that the main global dynamics can be determined without knowing the detailed local properties of the top surface, except of what is represented by the large singular values. In the bottom

row of Figure 8, the parameter and response singular vector is shown. The left panel, parameter singular vector, shows the changes in elevation that have most significant impact on the plume evolution until year 10. The plume thickness is shown in the upper left corner. The response eigenvector, right, shows most significant response. We note that this depends on that the norm for changes is the L_2 norm. We clearly identify the maximum of this parameter singular vector to be the dominating spill point at this time, i.e., year 10. The response of increasing the depth of the spill point is represented by the response singular vector (see left corner), and clearly shows that it will decrease the leakage out of the bar and increase the CO_2 height before the point. From a simple physical perspective in the limit of gravity-dominated flow, this could be anticipated beforehand. However, we point out that our methodology is not limited to this case and thus demonstrate the power of identifying the main contributions to dynamics with respect to the chosen quantities, purely by looking at the linearizion in terms of sensitivities of the complex the full system.

5. Sensitivity to parameter changes

The sensitivities related to porosity, density, permeability, and rate must be handled with particular care since these variables are of different character even if we have chosen to define all of them as dimensionless multiplication factors of the original values. The starting point for this discussion is to consider the top surface as constant so that the changes in CO_2 thickness can be written as

$$\mathrm{d}h = A_{m,t}\mathrm{d}\theta_m, \tag{41}$$

where m indicates the multiplicative variable of the parameter θ. First, we calculate the SVD of $A_{m,t} = U_{m,t}S_{m,t}V_{m,t}s$ at year 10, which gives

$$V_{m,t} = \begin{bmatrix} -0.6804 & -0.3839 & -0.3228 & -0.5343 \\ 0.0512 & -0.5841 & 0.7998 & -0.1288 \\ -0.0505 & 0.6617 & 0.3830 & -0.6426 \\ 0.7293 & -0.2714 & -0.3308 & -0.5339 \end{bmatrix}, \quad S_{m,t} = \begin{bmatrix} 87.0620 & 0 & 0 & 0 \\ 0 & 30.5161 & 0 & 0 \\ 0 & 0 & 2.1075 & 0 \\ 0 & 0 & 0 & 0.0909 \end{bmatrix}. \tag{42}$$

We identify the singular values which are significantly smaller than the others, as done in Section 4.2 with the eigenvalues of the Hessian. Again, a redefinition to a linear combination in the same way as in (35) and (36) of the parameter singular vector,

$$\tilde{v}_3 = v_4 - \frac{v_{4,i}}{v_{3,i}}v_3 = [-0.0131, -1.4197, -1.2608, 0]^T \propto [0, 1.13, 1, 0]^T, \tag{43}$$

$$\tilde{v}_4 = v_4 - \frac{v_{4,j}}{v_{3,j}}v_3 = [-0.5862, 0, -0.5809, -0.5872]^T \propto [1, 0, 1, 1]^T, \tag{44}$$

give a representation of the invariant scaling of the system. We note that $\frac{\tilde{v}_{3,2}}{\tilde{v}_{3,3}} = 1.13 \approx \left(\frac{\rho_w}{\rho_g} - 1\right)$. This near rank deficiency of $A_{m,t}$ is a consequence of only considering the h variable and it highlights the need to add alternative measurements which is sensitive to other aspects of the system. In a later section, we will discuss gravity measurements and uplift measurements.

6. Adding other measurements

We have shown that for the Sleipner case, the attempt to measure quantities only depending on the plume thickness resulted in two singular values that are small or zero. This shows that there is a need for more information in terms of additional measurements or other assumptions. In the case of additional knowledge about the pressure and the temperature, the equation of state (EQS) for CO_2 will lead to a density constraint. However, from Table 2, we see that even small changes in the assumption give very large differences in the estimated values. Given the large sensitivity to density changes of the system if the other parameters are kept constant, this assumption has limited value.

Another type of measurement is gravity changes, which also has been measured at Sleipner. A full treatment of gravity measurements in this case will require us to model all of the CO_2 layers, since gravity has a limited ability to differentiate in space. Gravity measurements depend directly on the CO_2 density, which is one of the missing parts
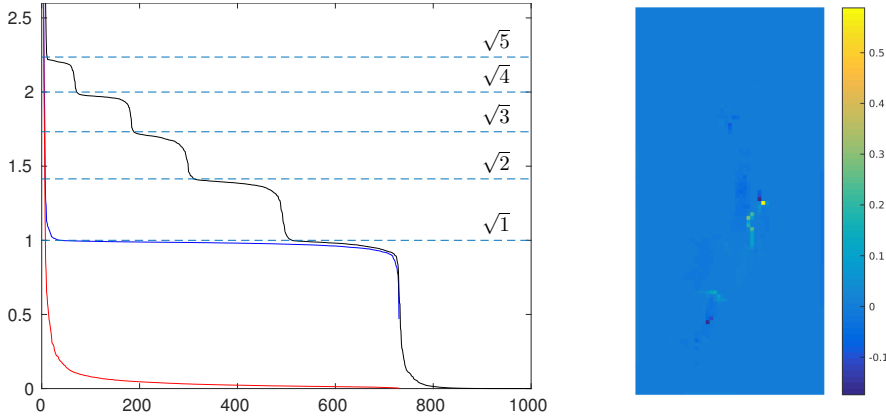
Fig. 9: The singular values of the full sensitivity. Only the singular values dominated by the top surface change dz is shown. The black line includes all time steps, while the blue line only includes year 12. Red line is the singular values of the sensitivities of $h + z$ at year 12. The value for the two highest singular values associated with changes in the global parameters for the full system was 146 and 55. Only cells where the CO_2 plume had a height larger than 1 meter was considered.

of the plume measurements. For measurements at the top of the overburden, gravity changes will very accurately be approximated with

$$d\mathbf{g}(\mathbf{r}_i) = \sum_j G_g(r_i - r_j)d(\Delta\rho h_j a_j \phi). \tag{45}$$

We recognize this one part of the second invariance, which also depends on the density difference between CO_2 and water. If we further simplify and assume $G_g(r_i - r_j)$ to be constant, we can approximate the change in gravity by

$$d\mathbf{g}(\mathbf{r}_i) = Cd(\Delta\rho\phi V_g) = Cd(\Delta\rho q_g)$$
$$= C(\Delta\rho Q_g)(dm_q - \frac{\rho_g}{\Delta\rho}dm_\rho), \tag{46}$$

where Q_g is the total injected volume of CO_2. This results in an equation representing a global measurement of changes in gravity as

$$dg = C(\Delta\rho Q_g)[0, 1, -\frac{\Delta\rho}{\rho_g}, 0, 0]d\theta, \tag{47}$$

which will restrict the null space of the matching function.

Another measurement that may be of use if pressure build up is large, is uplift measurements at the top of the overburden. This can be obtained with high precision and has shown to be of value at In Salah [21], where significant pressure buildup is present. Compared to gravity measurement, uplift is sensitive to the pressure even in the limit of assuming incompressibility. However, it is not sensitive to the exact scaling, see (20), since in this case the pressure does not change. As with gravity measurements, uplift has small sensitivity to details at the aquifer level because it is based on responses at a distance given by sums of Greens function of an elliptic equation. However, due to boundary condition, the responses are a bit more local, which is similar to the localization of the poro-elastic coupling response [22]. Uplift has limited value for Sleipner because the pressure changes are expected to be small.

6.1. The value of time measurements

A powerful aspect of having calculated all the sensitivities to the different times is that we can investigate the combined sensitivities to measurements at different times. In the following we will study the pure sensitivities, where h and dz are in scale of meters and the change in the other parameters is relative to the given value. If we include all CO_2 thicknesses of more than 1, we find that the two highest singular values are 100 and 40 for the last step, or 146 and 55 if all time intervals are consider, corresponding to 730 and 1735 heights considered, respectively. This can be compared with the Euclidean norm of the two sensitivity matrices of 111 and 163. The ratio of the largest singular

value, the smallest singular values, the norms and the square root of the ratio between the number of points are 1.46, 1.38, 1.47 and 1.54. This shows that the increase in resolution is less than ideal as expected, but that including all the measurements gives a significant increase in the estimated accuracy. Whether under other constraints this is worth the extra effort will be important for evaluation monitoring strategies.

We now investigate the singular values associated with the topography changes. Figure 9 shows the singular values for including time steps of year 3, 6, 8, 10 and 12, black, the singular values including only year 12, blue, and the singular values for sensitives of $h + z$ at year 12, red. We again notice that the CO_2–water interface only depends on a few singular values, while h depends on the full system. Furthermore, we notice that with our assumption of independent measurements, the sensitivity is well approximated in the sense that it depends linearly on the square root of the number of times instances in which a plume covers the cell. This would have been the ideal case if we considered each fit as an independent measurement of the top surface. Our interpretation is that using the physical model to estimate the top surface from the plume height acts like an ideal measurement and there is little information loss due to dependencies in the physical processes. The locality of the top-surface sensitivities in this case can be attributed to the fast time scale of obtaining the smooth surface. We also notice that there are a few singular values that are significantly higher than $\sqrt{5}$. These parameter singular vectors are dominated by spatial changes associated with a spill point. The parameter singular value corresponding the largest of them is shown in right panel of Figure 9. Compared with the other singular values, the parameter and the response singular values have a more global behavior.

7. Conclusion

In this work we have shown how a combination of VE simulation techniques and adjoint-based sensitivities can be used to estimate physical parameters from measurement data. As an example, we used plume heights reported in the literature for the Sleipner injection site to demonstrate our framework. The Hessian of the matching function was investigated to determine the parameters which was not constrained by the matching function. We explained this in terms of invariant scaling of the full system with regard to the plume thickness. One of these invariants was exact, while the other depends on an assumption of near incompressible dynamics, i.e. that pressure does not change the parameters of the system. Furthermore, we constructed the full sensitivity matrix relating changes in input parameters to changes in plume thickness. This full sensitivity matrix was used to identify the most important responses of the system using singular value decomposition. We showed that the singular values can be used to investigate the accuracy of the matched parameters with respect to uncertainty in the measured quantities. By a variable transformation, we pointed out that the dynamics of the water-CO_2 contact is much less sensitive to the top-surface topography. This both demonstrate that measurements of plume height is efficient to estimate the caprock topography and that in the case that the CO_2-water contact is the important quantity less information/measurements is needed.

For the CO_2-water interface, a compact representation of the linear sensitivities could be found by using SVD. The most significant singular vectors corresponded to elevation changes at effective spill-point, i.e., saddle point in the topography and the corresponding changes to changes in CO_2 between the corresponding compartments. This demonstrates the power of the combination of sensitivities and SVD in this setting.

We believe that the methodology introduced in this paper will be valuable to assess and design monitoring strategies for CO_2 injection sites. In our paper, we restricted much of the discussion to the linear domain. The power of this is that combinations of the linear sensitivity and assumed linear relations for measurements could be used to investigate different combinations of measurements and accuracy without doing full simulations. This could be used to find the most efficient measurements, which then later can be evaluated by full simulation.

Acknowledgements

References

[1] E. K. Halland, W. T. Johansen, F. Riis (Eds.), CO$_2$ Storage Atlas: Norwegian North Sea, Norwegian Petroleum Directorate, P. O. Box 600, NO–4003 Stavanger, Norway, 2011.
URL http://www.npd.no/no/Publikasjoner/Rapporter/CO2-lagringsatlas/

[2] A. Romdhane, E. Querendez, CO2 characterization at the Sleipner field with full waveform inversion: Application to synthetic and real data, Energy Procedia 63 (2014) 43584365. doi:10.1016/j.egypro.2014.11.470.

[3] B. Dupuy, S. Garambois, A. Asnaashari, H. M. Balhareth, M. Landrø, A. Stovas, J. Virieux, Estimation of rock physics properties from seismic attributes part 2: Applications, Geophysics 81 (4) (2016) M55M69. doi:10.1190/geo2015-0492.1.

[4] A. J. Cavanagh, R. S. Haszeldine, B. Nazarian, The Sleipner CO2 storage site: using a basin model to understand reservoir simulations of plume dynamics, First Break 33 (June) (2015) 61–68.

[5] V. Singh, A. Cavanagh, H. Hansen, B. Nazarian, M. Iding, P. Ringrose, Reservoir modeling of CO2 plume behavior calibrated against monitoring data from Sleipner, Norway, in: SPE Annual Technical Conference and Exhibition, Florence, Italy, 2010. doi:10.2118/134891-MS.

[6] H. M. l. Nilsen, P. a. Herrera, M. Ashraf, I. Ligaarden, M. Iding, C. Hermanrud, K. A. Lie, J. M. Nordbotten, H. K. Dahle, E. Keilegavlen, Field-case simulation of CO2-plume migration using vertical-equilibrium models, Energy Procedia 4 (2011) 3801–3808. doi:10.1016/j.egypro.2011.02.315.

[7] A. Cavanagh, Benchmark calibration and prediction of the Sleipner CO2 plume from 2006 to 2012, Energy Procedia 37 (2013) 3529–3545. doi:10.1016/j.egypro.2013.06.246.

[8] A. J. Cavanagh, R. S. Haszeldine, The Sleipner storage site: Capillary flow modeling of a layered CO2 plume requires fractured shale barriers within the Utsira Formation, International Journal of Greenhouse Gas Control 21 (2014) 101–112. doi:10.1016/j.ijggc.2013.11.017.

[9] A. Cavanagh, B. Nazarian, A new and extended Sleipner benchmark model for CO2 storage simulations in the Utsira formation, Energy Procedia 63 (2014) 2831–2835. doi:10.1016/j.egypro.2014.11.305.

[10] K. W. Bandilla, M. a. Celia, E. Leister, Impact of model complexity on CO2 plume modeling at Sleipner, Energy Procedia 63 (2014) 3405–3415. doi:10.1016/j.egypro.2014.11.369.

[11] G. Zhang, P. Lu, C. Zhu, Model predictions via history matching of CO2 plume migration at the Sleipner project, Norwegian North Sea, Energy Procedia 63 (2014) 3000–3011. doi:10.1016/j.egypro.2014.11.323.

[12] C. Zhu, G. Zhang, P. Lu, L. Meng, X. Ji, Benchmark modeling of the Sleipner CO2 plume: Calibration to seismic data for the uppermost layer and model sensitivity analysis, International Journal of Greenhouse Gas Control 43 (2015) 233–246. doi:10.1016/j.ijggc.2014.12.016.

[13] H. M. Nilsen, K.-A. Lie, O. Andersen, Robust simulation of sharp-interface models for fast estimation of CO$_2$ trapping capacity, Computational Geosciences 20 (1) (2016) 93–113. doi:10.1007/s10596-015-9549-9.
URL http://dx.doi.org/10.1007/s10596-015-9549-9

[14] H. M. Nilsen, K.-A. Lie, O. Andersen, Fully implicit simulation of vertical-equilibrium models with hysteresis and capillary fringe, Computational Geosciences 20 (1) (2016) 49–67. doi:10.1007/s10596-015-9547-y.
URL http://dx.doi.org/10.1007/s10596-015-9547-y

[15] J. D. Jansen, Adjoint-based optimization of multi-phase flow through porous media – a review, Computers & Fluids 46 (1, SI) (2011) 40–51. doi:10.1016/j.compfluid.2010.09.039.

[16] R. Chadwick, D. J. Noy, History-matching flow simulations and time-lapse seismic data from the Sleipner CO2 plume, in: Proceedings of the 7th Petroleum Geology Conference, Geological Society, London, 2010, pp. 1171–1182. doi:10.1144/0071171.

[17] A. K. Furre, O. Eiken, Dual sensor streamer technology used in Sleipner CO2 injection monitoring, Geophysical Prospecting 62 (5) (2014) 1075–1088. doi:10.1111/1365-2478.12120.

[18] R. Allen, H. Nilsen, O. Andersen, K.-A. Lie, On obtaining optimal well rates and placement for co2 storage, in: ECMOR XV – 15th European Conference on the Mathematics of Oil Recovery, EAGE, 2016. doi:10.3997/2214-4609.201601823.

[19] I. H. Bell, J. Wronski, S. Quoilin, V. Lemort, Pure and pseudo-pure fluid thermophysical property evaluation and the open-source thermophysical property library coolprop, Industrial and Engineering Chemistry Research 53 (6) (2014) 2498–2508. doi:10.1021/ie4033999.

[20] R. Span, W. Wagner, A new equation of state for carbon dioxide covering the fluid region from the triple-point temperature to 1100 k at pressures up to 800 mpa, Journal of physical and chemical reference data 25 (6) (1996) 1509–1596.

[21] P. Ringrose, A. Mathieson, I. Wright, F. Selama, O. Hansen, R. Bissell, N. Saoula, J. Midgley, The in salah co2 storage project: Lessons learned and knowledge transfer, Energy Procedia 37 (2013) 6226 – 6236. doi:http://dx.doi.org/10.1016/j.egypro.2013.06.551.
URL http://www.sciencedirect.com/science/article/pii/S1876610213007947

[22] O. Andersen, H. Nilsen, S. Gashda, Modelling geomechanical impact of co2 injection and migration using precomputed response functions, in: ECMOR XV – 15th European Conference on the Mathematics of Oil Recovery, EAGE, 2016. doi:10.3997/2214-4609.201601760.